ORIGINAL ARTICLE

Calculation method of convective heat transfer coefficients for thermal simulation of a spindle system based on RBF neural network

Dianxin Li · Pingfa Feng · Jianfu Zhang · Zhijun Wu · Dingwen Yu

Abstract Results from the temperature field and thermal deformation simulation of a spindle system are greatly affected by the accuracy of convective heat transfer coefficients (CHTCs). This paper presents a new method based on radial basis function (RBF) neural network to calculate CHTCs. First, the temperature field and thermal deformations of a spindle system were obtained by experimental and finite-element (FE) methods. However, the simulation results are significantly different from the experimental results because boundary conditions used for the FE model were derived empirically. Second, the relationship between the simulated temperature values and CHTCs were established by a RBF neural network. Using the experimental temperature values as an input vector of the RBF neural network, CHTCs of the spindle system can be predicted through an iterative calculation taking 14 cycles. Finally, the effectiveness of the proposed method was proved using steady-state and transient-state analyses of the spindle system. Results from the steady-state simulation show that temperature errors were less than 4 % at the seven thermal-critical points and deformation errors in the three directions were less than 6 %. Results from the

transient-state simulation of the spindle system show that the variations for each of the thermal characteristics are in good agreement with the experimental results. The method provides guidance for modifying boundary conditions of a FE model.

1 Introduction

Among many factors affecting workpiece errors in precision machining, thermal errors can cause up to 70 % of manufacturing errors [1–3]. Furthermore, the spindle system (the spindle assembly and the headstock) is one of the biggest sources of thermal errors [4–6]. Currently, no theoretical analysis can predict the thermal characteristics (temperature field and thermal deformation) of a spindle system with sufficient accuracy. Experimental and finite-element (FE) methods are the primary methods for researching thermal characteristics of spindle systems. To measure these thermal characteristics, a large number of sensors are needed. Consequently, the creation of an accurate experimental platform is a difficult and time-consuming task. Even so, it is impossible to acquire all thermal characteristics of the spindle system. At the design stage of a machine tool, FE methods can predict all thermal characteristics of the spindle system. However, under most circumstances, simulation results are significantly different from actual values because of complicated boundary conditions of the FE model. Therefore, there is a critical need to develop an accurate FE model by modifying boundary conditions. Use of this model cannot only predict all thermal characteristics of the spindle system, but also reduce the huge

D. Li (✉) · P. Feng · J. Zhang · Z. Wu · D. Yu
Department of Mechanical Engineering, Tsinghua University,
Room 2502, Building 9003, Haidian District, Beijing 100084,
People's Republic of China
e-mail: lidx11@mails.tsinghua.edu.cn

P. Feng
e-mail: fengpf@mail.tsinghua.edu.cn

J. Zhang
e-mail: zhjf@tsinghua.edu.cn

Z. Wu
e-mail: wuzhijun@mail.tsinghua.edu.cn

D. Yu
e-mail: yudw@mail.tsinghua.edu.cn

effort needed in experimental verification and design costs in prototype optimizing.

Accuracy of the FE model is affected by a whole range of boundary conditions, such as heat sources, thermal contact resistances, and convective heat transfer coefficients (CHTCs). The spindle bearing is the main thermal source of the spindle system, and heat can be computed by the mature method presented in [7]. The thermal contact resistances between different machine parts can be obtained by experimental [8, 9] or theoretical [10, 11] methods. CHTCs reflect the heat transfer capability between surfaces of the spindle system and fluids. However, these cannot be measured directly because each is related not only to fluid properties, fluid velocity, and shape of the heat transfer surface, but also to the temperature difference between the heat transfer surface and fluid. Although no precise rule applies for calculating CHTCs, the associated boundary conditions are the most important in the FE model [12]. The convective heat transfer of a spindle system can be classified as forced and natural. Yang [13] proposed a method to calculate the forced CHTC of a rotating spindle and the natural CHTC when the spindle stops rotating. Jiang [14] calculated the forced CHTC of a spindle system by assuming the air flowing through the spindle system is forced turbulent air, and the natural CHTC was determined based on empirical values. Chen [15] calculated the CHTCs on every surface of a hydrostatic spindle from equations deduced from the literature.

The existing thermal simulation models mainly considered the natural convection around stationary surfaces and the forced convection heat transfer between rotating surfaces and the air, but rarely considered the forced convection heat transfer between cooling fluid and cooling troughs. Besides, empirically determined equations are usually imposed in calculating CHTCs. All of the above drawbacks resulted in poor simulation accuracy of the spindle system. Much research work has focused on improving the calculation accuracy of CHTCs. Wu [16] presented a method of calculation for spindle systems based on experimental data and significance tests. Fan [17] presented an inverse method based on thermographic temperature measurements, and the distribution of CHTCs for a flat plate surface was estimated by iteratively calculating temperature distribution equations. Rebay [18] developed a pulsed photothermal method for measuring the CHTC between an air flow and a heated slab surface. However, in general, the abovementioned approaches have limitations such as high computational burden, low accuracy, and complicated experimental systems.

To calculate the CHTCs accurately and quickly to improve the simulation accuracy of the spindle system, we first constructed an experimental test and a FE simulation for thermal characteristics of a spindle system. Furthermore, the relationship between the simulated temperature values and the CHTCs were established by a RBF neural network. We then used the experimental temperature values as input to the neural network to calculate the CHTCs. Finally, the effectiveness of the proposed method was proved by steady-state and transient-state analyses of the spindle system.

2 Thermal test of a spindle system

As depicted in Fig. 1, a machining center consists of a table, saddle, bed, column, headstock, baffle, spindle motor, and spindle assembly. To accurately measure the deformations of the spindle system, a test bar was assembled in the machining center. As shown in Fig. 2, two laser displacement sensors were fixed on the table to measure deformations of the test bar in the X- and Y-directions. An eddy current displacement sensor was placed at the bottom of the test bar to measure deformations of the test bar in the Z-direction. To get a precise temperature distribution of the spindle system, seven platinum resistance temperature sensors (T1–T7) were fixed on thermal-critical points of the surfaces. The machine tool was placed in a workshop with a constant temperature of 24 °C.

The spindle was rotated at a constant speed of 4,000 rpm with the cooling system turned on. The experiment took 5 h to reach a steady state. The temperature field and thermal deformation curves were measured in real-time. The test platform is shown in Fig. 3.

3 Development of the FE simulation model

The most important part of machine tool thermal analysis is the determination of the boundary conditions of the FE model. These conditions include the following: (1) establishment of the solid model, (2) determination of the material properties, (3) analysis of the thermal sources, (4) analysis of the thermal contact resistances, and (5) analysis of the CHTCs. We elaborate these key issues as follows.
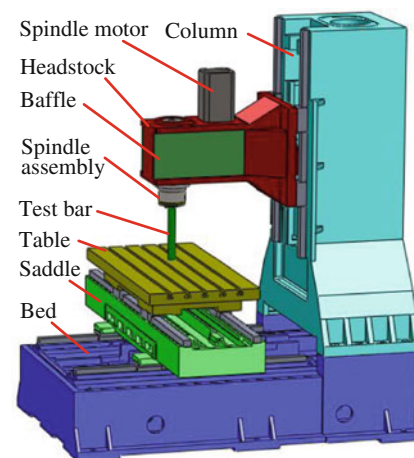

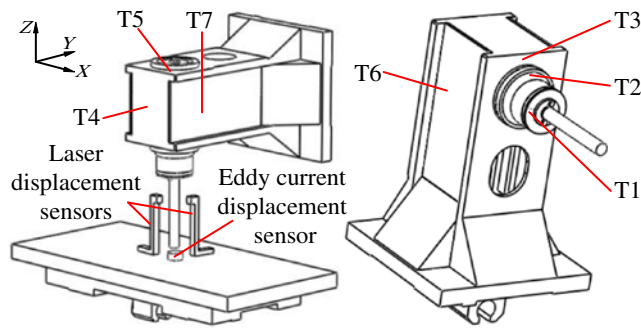Fig. 1 Solid model of the machine tool

Fig. 2 Arrangement of the sensors

Fig. 4 Structure of the spindle assembly

3.1 Establishment of the solid model

The structure of the spindle assembly is shown in Fig. 4, and only the key parts of the spindle assembly were considered. The structure of the headstock is shown in Fig. 5. The cooling troughs were arranged on both sides and at the front of the headstock. To actually consider thermal characteristics of the spindle system, the whole machine solid model (Fig. 1) was used for the FE simulation. The baffles were installed on both sides of the headstock, as shown in Fig. 1.

3.2 Determination of the material properties

The machine tool under research has five major materials, and these material properties were assigned to their respective structures in the FE analysis software. HT300 was applied to the bed, saddle, table, column, and headstock; 40Cr was applied to the spindle and guide ways; GCr15 was applied to the bearings; T10A was applied to the test bar; and steel was applied to the spindle sleeve, bearing sleeve, and spindle motor. The material properties are presented in Table 1. Small details such as holes, fillets, and chamfers were neglected. An automatic partitioning method for meshing was adopted, and meshing generated a total of 201,032 elements and 382,163 nodes (see Fig. 6).
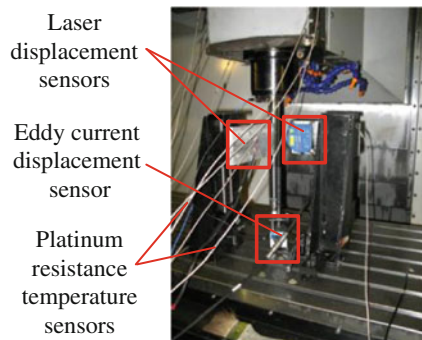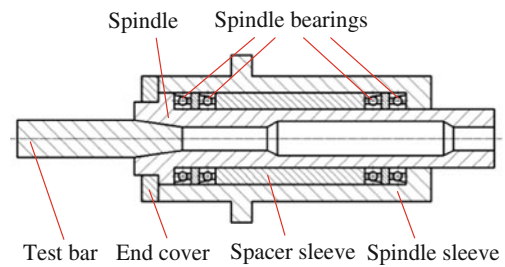
3.3 Thermal sources analysis

For the spindle system, the power loss of the spindle motor and the friction heat from the spindle bearing are the most important heat sources.

3.3.1 Heat generation in the motor

For this study, rated power of the spindle motor was 7.5 kW and a cooling fan was set on top of the spindle motor. Based on past experience, the power transferred from the motor to the headstock was approximately 30 W.

3.3.2 Computation of the spindle bearing friction heat

While the spindle bearings are in motion, friction heat was generated by the relative movements between the various parts of the bearing. The heat can be computed by the following Eq. (7):

$$H_f = 1.047 \times 10^{-4} nM \qquad (1)$$

Where H_f is the heat generated power (in watts), n is the rotating speed of the spindle (in revolutions per minute), and M is the total frictional torque of the bearing (in Newton per millimeter).

The total frictional torque M consists of two components and can be calculated using:
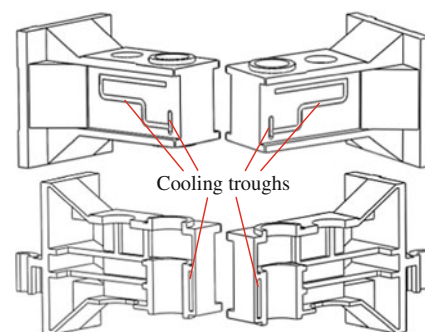
$$M = M_l + M_v \qquad (2)$$

Fig. 3 Thermal characteristics test platform

Fig. 5 Structure of the headstock

Table 1 Properties of the materials

Material	HT300	40Cr	GCr15	T10A	Steel	Air
Modulus of elasticity (GPa)	130	200	200	196	206	–
Poisson's ratio	0.24	0.3	0.28	0.3	0.28	–
Linear expansion coefficient (10^{-5} K^{-1})	1.10	1.13	1.20	1.21	1.20	–
Thermal conductivity (W m^{-1} K^{-1})	45	50.66	48	48	60.5	0.02454
Specific heat capacity (J kg^{-1} K^{-1})	510	477	729	480	434	1.005
Density (kg m^{-3})	7250	7850	7800	7800	7850	1.293

Where M_l is the mechanical friction torque (in Newton per millimeter) and M_υ is the viscous friction torque (in Newton per millimeter).

1. Computation of the mechanical friction torque

    The mechanical friction torque M_l depends on the structural parameters of the bearing and the applied load. M_l can be computed as follows:

    $$M_l = f_1 p_1 d_m \tag{3}$$

    Where f_1 is a coefficient related to the bearing type and load, p_1 is the bearing load (N), and d_m is the mean diameter of the bearing (in millimeters).
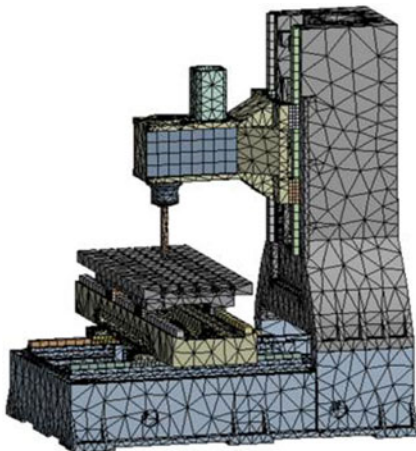
2. Computation of the viscous friction torque

    The viscous friction torque M_υ depends on the structural parameters of the bearing and viscosity of lubricant. M_υ can be computed as follows:

    $$M_v = 10^{-7} f_0 (\upsilon n)^{2/3} d_m^3 \quad \text{if} \quad \upsilon n \geq 2000 \tag{4}$$

    $$M_v = 160 \times 10^{-7} f_0 d_m^3 \quad \text{if} \quad \upsilon n < 2000 \tag{5}$$

Where f_0 is a coefficient related to the bearing type and lubrication method, and υ is the kinematic viscosity of the lubricant under working temperature (in square millimeters per second).

In this study, $\upsilon n \geq 2,000$ at the speed of 4,000 rpm, and Eq. (4) should be used. By combining parameters of the machine tool and Eqs. (2)–(4), friction heat of a single spindle bearing is 27.16 W.

3.4 Analysis of the thermal contact resistances

There are many joints existing in the spindle system, and these joints result in a temperature difference between the two contact surfaces. Such a temperature jump plays a significant role in the thermal simulation of the spindle system. In reality, the thermal contact resistance at the solid joints is mainly determined by contact pressure, contact medium, roughness of the surfaces, and material properties on both sides of the joint. In this study, thermal contact resistances at the main joints affecting thermal transfer in the spindle system were considered, i.e., the joint between the bearing inner ring and the spindle, the bearing outer ring and spindle sleeve, the spindle sleeve and headstock, the spindle taper hole and the test bar, and guideways between headstock and column. Values for these thermal contact resistances were obtained by experimental methods [9] (see Table 2).

3.5 Computation of the CHTCs

Convective heat transfer of the spindle system include forced convection heat transfer between rotating surfaces and the air, forced convection heat transfer between cooling fluid and the cooling troughs, and natural convection between stationary surfaces and the ambient air. These CHTCs are calculated initially by empirical equations.

Fig. 6 FE model of the machine tool

Table 2 Thermal contact resistances of key joints (m^2 K W^{-1})

Joint surface	Thermal contact resistance
Bearing inner ring–Spindle	1.37×10^{-4}
Bearing outer ring–Spindle sleeve	6.06×10^{-4}
Spindle sleeve–Headstock	1.13×10^{-3}
Spindle taper hole–Test bar	2.00×10^{-3}
Guideways between headstock and column	1.67×10^{-3}

Table 3 CHTCs of the FE model (W m^{-2} K^{-1})

CHTCs	h_s	h_t	h_c	h_f
Value	121.2	96.2	574.3	9.7

Table 4 Comparison of the temperature values

No. of the points	Simulated values (°C)	Experimental values (°C)	Simulation errors (%)
T1	29.11	28.7	1.41
T2	27.92	30.3	−8.52
T3	25.86	29.6	−14.46
T4	25.66	30.5	−18.86
T5	25.83	31.1	−20.40
T6	26.08	29.7	−13.88
T7	26.21	29.6	−12.93

3.5.1 Forced convection heat transfer between rotating surfaces and the air

The rotating bodies exposed to the air, such as the spindle and test bar, produced relative movement between the outer surfaces and the nearby air. The forced CHTC can be calculated using the following equation [19]:

$$h_{air} = \frac{Nu_{air}\lambda_{air}}{d_s} \quad (6)$$

Where Nu_{air} is the Nusselt number, λ_{air} is the thermal conductivity of the air (watts per meter Kelvin), and d_s is the equivalent diameter of the rotating surface (in millimeters).

The Nusselt number Nu_{air} can be calculated as follows:

$$Nu_{air} = 0.133 Re_{air}^{2/3} Pr_{air}^{1/3} \quad (7)$$

Where Re_{air} is the Reynolds number obtained from Eq. (8) and Pr_{air} is the Prandtl number obtained from Eq. (9) as follows:

$$Re_{air} = \frac{v_{air}d_s}{\upsilon_{air}} \quad (8)$$

$$Pr_{air} = \frac{C_{air}v_{air}}{k_{air}} \quad (9)$$

Where v_{air} is the velocity, υ_{air} is the kinematic viscosity, C_{air} is the specific heat capacitance, and k_{air} is the dynamic viscosity of the air.

By Eqs. (6)–(9), the forced CHTCs of the spindle surface and the test bar surface are h_s =121.2 W m^{-2} K^{-1} and h_t = 96.2 W m^{-2} K^{-1}, respectively.
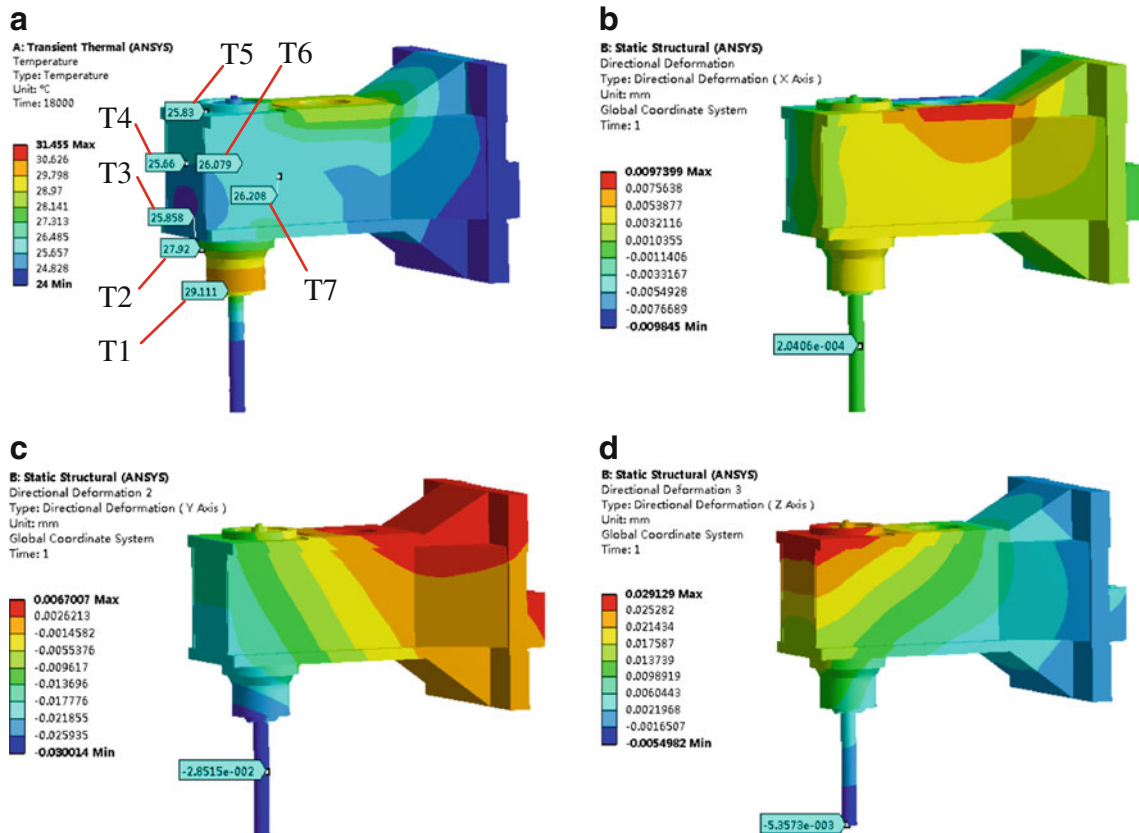

Fig. 7 Simulation results of the spindle system

Table 5 Comparison of the thermal deformations

Deformation direction	Simulated values (μm)	Experimental values (μm)	Simulation errors (%)
X	0.20	5.05	−96.04
Y	28.52	31.68	−9.98
Z	5.36	28.76	−81.36

3.5.2 Forced convection heat transfer between cooling fluid and the cooling troughs

The flow states of the cooling fluid inside the cooling troughs are categorized as laminar flow state, turbulent state, and transition state. The flow states for the fluid can be judged based on the fluid Reynolds' number, Re_f, as shown in Eq. (10) [20]:

$$Re_{\text{fluid}} = \frac{v_{\text{fluid}} D_H}{\upsilon_{\text{fluid}}} \tag{10}$$

Where v_{fluid} is the velocity of the cooling fluid, D_H is the equivalent diameter of the cooling troughs, and υ_{fluid} is the kinematic viscosity of the fluid. In this study, $Re_{\text{fluid}}=1,086.0$, and the Nusselt number of the fluid can be calculated as follows:

$$N_{u_f} = 1.86\left(Re_{\text{fluid}} Pr_{\text{fluid}} \frac{D_H}{L}\right)^{1/3} \tag{11}$$

Where L is length of the troughs and Pr_{fluid} is the Prandtl number obtained as follows:

$$Pr_{\text{fluid}} = \frac{C_{\text{fluid}} v_{\text{fluid}}}{k_{\text{fluid}}} \tag{12}$$

Where C_{fluid} and k_{fluid} are the specific heat capacitance and dynamic viscosity of the cooling fluid.
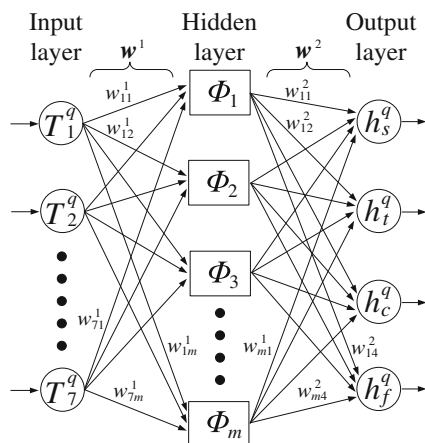

Fig. 8 The RBF neural network structure

Table 6 The target matrix (W m^{-2} K^{-1})

Serial no.	1	2	3	4	5	6
Ratio	1.2	1	0.8	0.6	0.4	0.2
h_s	145.44	121.2	96.96	72.72	48.48	24.24
h_t	115.44	96.2	76.96	57.72	38.48	19.24
h_c	689.16	574.3	459.44	344.58	229.72	114.86
h_f	11.64	9.7	7.76	5.82	3.88	1.94

The forced CHTC between cooling fluid and the cooling troughs can be calculated as follows:

$$h_c = \frac{Nu_{\text{fluid}} \lambda_{\text{fluid}}}{D_H} \tag{13}$$

Where λ_{fluid} is the thermal conductivity of the fluid (watts per meter Kelvin).

From Eqs. (10)–(13), the forced CHTC between cooling fluid and the cooling troughs is $h_c=574.3$ W m^{-2} K^{-1}.

3.5.3 Natural convection around stationary surfaces

For natural convection around stationary surfaces exposed to air, such as stationary surfaces of the spindle system and other machine tool parts, $h_f=9.7$ W m^{-2} K^{-1} was used [19].

The CHTCs of the FE model are shown in Table 3.

4 Thermal simulation of the spindle system

All simulations were performed as transient thermal simulations. The initial temperature for the whole machine was set to 24 °C and the step end time was set to 18,000 s. Boundary conditions obtained from Sect. 3 were applied to the FE model to obtain the temperature field of the whole machine. Based on the temperature field, as well as fixing the bottom of the bed by a displacement constraint, thermal deformations of the whole machine in each of the three independent directions were obtained. To highlight thermal characteristics of the spindle system, other parts of the machine tool were hidden.

Table 7 The input matrix (°C)

Serial no.	1	2	3	4	5	6
T1	28.09	29.85	30.22	30.35	31.17	31.82
T2	29.03	29.77	30.29	30.12	31.16	31.80
T3	24.21	25.87	27.25	29.47	31.97	33.52
T4	23.99	24.66	26.35	28.96	31.76	33.85
T5	24.05	25.84	27.28	29.58	32.05	34.68
T6	24.68	26.47	27.93	29.08	30.67	31.43
T7	25.52	26.22	27.99	29.07	30.57	31.35

Table 8 Calculation process of the CHTCs (W m^{-2} K^{-1})

Calculation times	h_s	h_t	h_c	h_f
1	96.67	81.77	378.85	4.66
2	172.09	115.81	582.94	11.64
3	50.08	63.49	383.37	2.89
4	157.14	101.99	588.05	13.91
5	54.81	57.56	318.36	2.98
6	126.16	90.75	421.09	14.56
7	72.88	72.26	343.35	7.08
8	123.26	94.19	474.90	8.10
9	92.88	62.25	352.15	5.08
10	118.28	91.03	453.53	9.80
11	107.46	75.25	393.24	9.10
12	102.01	87.28	438.37	9.03
13	106.78	70.66	409.15	9.57
14	108.48	74.53	424.63	9.01

Figure 7a shows the simulated temperature values at the measuring positions. Figure 7b–d shows the simulated deformations at the measuring positions in the X-, Y-, and Z-directions.

Table 4 shows the comparison of simulated and measured temperature values at the defined positions. Table 5 shows the comparison of simulated and measured deformations in the X-, Y-, and Z-directions. It can be seen that the simulation results are significantly different from the experimental results. Therefore, boundary conditions of the FE model should be modified. By modifying the CHTCs listed in Table 3, this paper presents a method that can be used to improve the simulation accuracy of the spindle system.

5 Calculation of the CHTCs based on RBF neural network

There exists a multi-input, multi-output nonlinear relationship between the simulated thermal characteristics of the spindle system and the CHTCs. It is well known that a nonlinear system can be well approximated by the RBF neural network [21, 22]. Based on the simulation results, this paper established a RBF neural network reflecting the relationship between the simulated temperature values and the CHTCs. Using the experimental temperature values as input to the neural network, the corresponding CHTCs can be obtained.
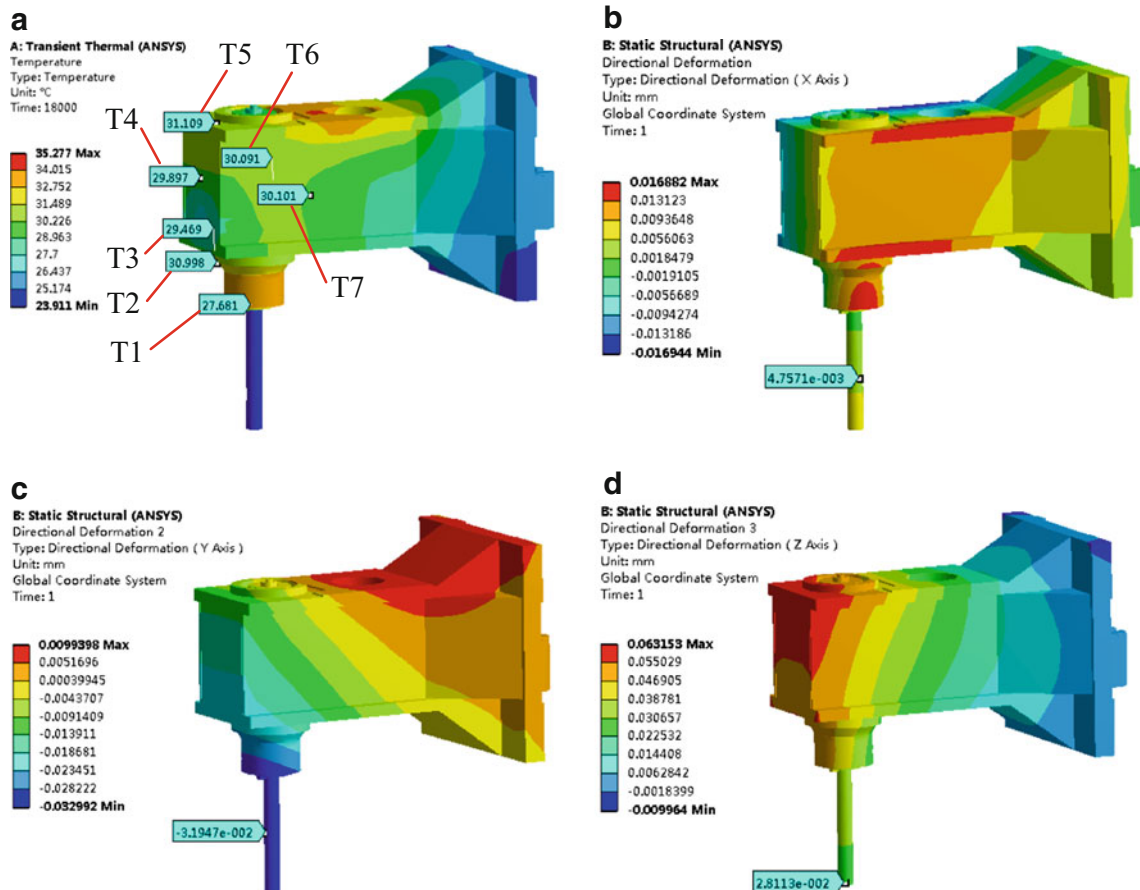

Fig. 9 Modified simulation results of the spindle system

Table 9 Comparison of the temperature values

No. of the points	Simulated values (°C)	Experimental values (°C)	Simulation errors (%)
T1	27.68	28.7	−3.55
T2	31.00	30.3	2.31
T3	29.47	29.6	−0.44
T4	29.90	30.5	−1.97
T5	31.11	31.1	0.03
T6	30.09	29.7	1.31
T7	30.10	29.6	1.69

Fig. 10 Comparison of the temperature values

5.1 Structure of the RBF neural network

As shown in Fig. 8, the RBF neural network consists of an input layer, a hidden layer, and an output layer. Here, $T^q = [T_1^q, T_2^q, \cdots, T_7^q]^T$ is the q th input vector of the network, w_1 is the connecting weight between the hidden layer and the input layer, Φ_j is the activation function, usually Gaussian, of the radial units [23, 24], w_2 is the connecting weight between the hidden layer and the output layer, and $h^q = [h_s^q, h_t^q, h_c^q, h_f^q]^T$ is the output vector of the network, namely the predicted CHTCs.

5.2 Establishment of the RBF neural network

The target matrix, input matrix, and spread of the RBF are needed for the establishment of a RBF neural network.

1. The target matrix

    As shown in Tables 4 and 5, the simulation value of T1 is in good agreement with the experimental result. However, the simulation values of T2–T7 and deformations of the spindle system are much less than the experimental results. To increase the simulation values, the CHTCs listed in Table 3 should be decreased to reduce heat transfer between the spindle system and the fluids. The designed target matrix is shown in Table 6, where group 2 is the theoretical values, i.e., the CHTCs listed in Table 3. Group 1 is 1.2 times those in group 2; group 3, 4, 5, and 6 are 80, 60, 40, and 20 % of the theoretical values, respectively. The target matrix can be written as $h = [h^1, h^2, \cdots, h^6]$.

2. The input matrix

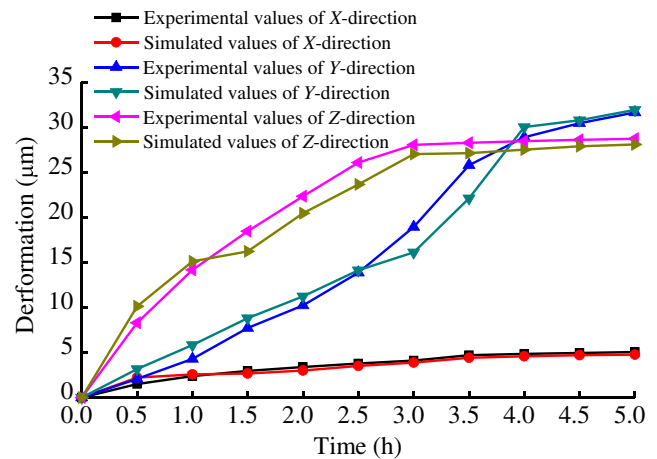   Boundary conditions of the heat sources, thermal contact resistances, and CHTCs listed in Table 6 were applied

to the FE model. As shown in Table 7, the simulated temperature values of T1–T7 compose the input matrix of the neural network. The input matrix can be written as $T = [T^1, T^2, \cdots, T^6]$.

3. Spread of the RBF

    While establishing the RBF neural network implemented on Matlab, spread=1 is used [25, 26].

    According to the above description, the established RBF neural network is as follows:

$$\text{spread} = 1; \text{net} = newrbe(T, h, 1) \qquad (14)$$

    Where *newrbe*, the create function of the RBF neural network, is used to train the RBF neural network with input matrix **T** and target matrix **h**.

5.3 Calculation steps of the CHTCs

According to the established RBF neural network and the temperature test results, calculation steps of the CHTCs are as follows:
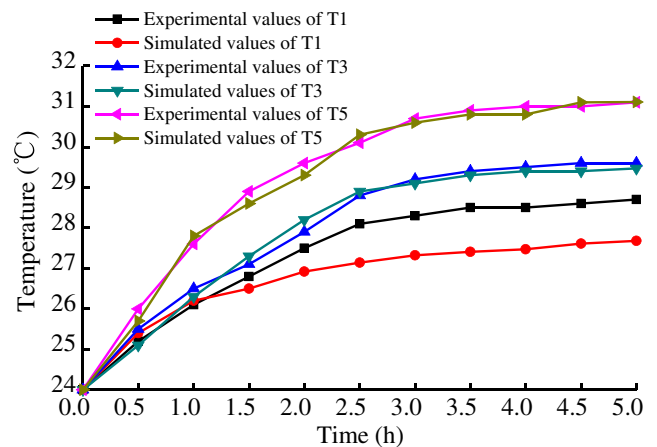
Table 10 Comparison of the thermal deformations

Deformation direction	Simulated values (μm)	Experimental values (μm)	Simulation errors (%)
X	4.76	5.05	−5.74
Y	31.95	31.68	0.85
Z	28.11	28.76	−2.06

Fig. 11 Comparison of the thermal deformations

Step 1 The temperature test result $\boldsymbol{T}' = [T_1', T_2', \cdots, T_7']^{\mathrm{T}}$ is used as the input vector of the RBF neural network, and the CHTCs can be predicted as follows:

$$\widehat{h}^{m} = sim\,(net, T') \qquad (15)$$

Where sim is the calculation function of the neural network, and $\widehat{h}^{m} = \left[\widehat{h}_s^m, \widehat{h}_t^m, \widehat{h}_c^m, \widehat{h}_f^m\right]^{\mathrm{T}}$ is the CHTCs calculated by the neural network.

Step 2 Substituting the heat sources, thermal contact resistances and $\widehat{h}^{m} = \left[\widehat{h}_s^m, \widehat{h}_t^m, \widehat{h}_c^m, \widehat{h}_f^m\right]^{\mathrm{T}}$ calculated by step 1 into the FE model to determine the simulated temperature value of $T^m = [T_1^m, T_2^m, \cdots, T_7^m]^{\mathrm{T}}$

Step 3 Let $e^m = [e_1^m, e_2^m, \cdots, e_7^m]^{\mathrm{T}}$, where $\boldsymbol{e}_j^m = \frac{\left|T_j^m - T_j'\right|}{T_j'}, j = 1, 2, \cdots, 7$. If $e_j^m < 0.05$, then turn to step 5; otherwise, turn to step 4.

Step 4 Add T^m to $T = [T^1, T^2, \cdots, T^6]$ which extends to $T^{m+1} = [T^1, T^2, \cdots, T^6, T^m]$. Add $\widehat{h}^{m}$ to $h = [h^1, h^2, \cdots, h^6]$ which extends to $\widehat{h}^{m+1} = \left[h^1, h^2, \cdots, h^6, h^m\right]$. By T^{m+1} and $\widehat{h}^{m+1}$ as well as Eq. (14), a new RBF neural network can be trained. Repeat steps 1–3.

Step 5 The calculation process ends and the final values of the CHTCs are obtained.

According to the above method, the CHTCs are obtained through a calculation taking 14 iterations. The outcomes of the calculation at each step are shown in Table 8.

6 Validation of the CHTCs

6.1 Validation of the steady-state analysis results

The initial temperature for the whole machine was set to 24 °C and the step end time was set to 18,000 s. Boundary conditions of the heat sources, thermal contact resistances, and $\widehat{h}^{14} = [108.48, 74.53, 424.63, 9.01]^T$ were applied to the FE model. Figure 9a shows the simulated temperature values at the measuring positions. Figure 9b–d shows the simulated deformations at the measuring positions in the X-, Y-, and Z-directions.

Table 9 shows the comparison of the modified simulation and measured temperature values at the defined positions. Table 10 shows the comparison of the modified simulation and measured deformations in the X-, Y-, and Z-directions. The modified simulation results are clearly in close agreement with the experimental results.

6.2 Validation of the transient-state analysis results

To further verify accuracy of the CHTCs, thermal characteristics variation process of the spindle system were simulated. The initial temperature for the whole machine was set to 24 °C and the step end time was set to 1,800, 3,600, 5,400, 7,200, 9,000, 10,800, 12,600, 14,400, 16,200, and 18,000 s, respectively. Boundary conditions of the heat sources, thermal contact resistances, and $\widehat{h}^{14}$ were applied to the FE model. Taking temperature values at T1, T3, and T5 as an example, comparison of the simulated and measured temperature values are shown in Fig. 10. Comparison of the simulated and measured deformations at the measuring positions in the X-, Y-, and Z-directions are shown in Fig. 11. Overall, the simulation results obtained using the modified CHTCs were in good agreement with the experimental results.

7 Conclusions

This paper proposed a method for modifying the CHTCs of a spindle system to improve the simulation accuracy of the thermal characteristics. A RBF neural network was established based on simulated temperature values and CHTCs. Using the experimental temperature values as input vector of the RBF neural network, CHTCs of the spindle system were obtained through an iterative calculation taking 14 cycles. The effectiveness of the proposed method was proved by steady-state and transient-state analyses of the spindle system. This method has the following advantages: (1) it is simple because the CHTCs can be predicted by a RBF neural network instead of modifying theoretical equations, (2) it only took 14 iterations of the calculation to get exact values of the CHTCs, and (3) the modified simulation results were consistent with the experimental results compared with empirical methods.

Nevertheless, this paper dealt only with the spindle system. To improve the thermal characteristics simulation accuracy of the whole machine tool, there is a need to address other machine parts all together, such as the ball screw feeding system. Future work will focus on the method to improve simulation accuracy of the whole machine tool.

References

1. Liang RJ, Ye WH, Zhang HH, Yang QF (2012) The thermal error optimization models for CNC machine tools. Int J Adv Manuf Technol 63(9–12):1167–1176

2. Han J, Wang LP, Cheng NB, Wang HT (2012) Thermal error modeling of machine tool based on fuzzy *c*-means cluster analysis and minimal-resource allocating networks. Int J Adv Manuf Technol 60(5–8):463–472

3. Wu H, Zhang HT, Guo QJ, Wang XS, Yang JG (2007) Thermal error optimization modeling and real-time compensation on a CNC turning center. J Mater Process Technol 207(1–3):172–179

4. Creighton E, Honegger A, Tulsian A, Mukhopadhyay D (2010) Analysis of thermal errors in a high-speed micro-milling spindle. Int J Mach Tools Manuf 50(4):386–393

5. Mori M, Mizuguchi H, Fujishima M, Ido Y, Mingkai N, Konishi K (2009) Design optimization and development of CNC lathe headstock to minimize thermal deformation. CIRP Ann Manuf Technol 58(1):331–334

6. Chen TY, Wei WJ, Tsai JC (1999) Optimum design of headstocks of precision lathes. Int J Mach Tools Manuf 39(12):1961–1977

7. Harris TA (1991) Rolling Bearing Analysis. John Wiley and Sons, New York

8. Xu RP, Feng HD, Zhao LP, Xu L (2006) Experimental investigation of thermal contact conductance at low temperature based on fractal description. Int Commun Heat Mass 33(7):811–818

9. Zhao HL, Huang YM, Xu JL, Jiang LY, Zhang WH, Sheng BH (1999) Experiment research on thermal contact resistance of normal used joints. J Xi'an Univ Technol 15(3):26–29 (in Chinese)

10. Ciavarella M, Dibello S, Demelio G (2008) Conductance of rough random profiles. Int J Solids Struct 45(3–4):879–893

11. Baïri A, Laraqi N (2005) Heat transfer across a solid-solid interface obtained by machining in a lathe. J Mater Process Technol 169(1):89–93

12. Neugebauer R, Ihlenfeldt S, Zwingenberger C (2010) An extended procedure for convective boundary conditions on transient thermal simulations of machine tools. Prod Eng 4(6):641–646

13. Yang ZY, Sun ML, Li WQ, Liang WY (2011) Modified Elman network for thermal deformation compensation modeling in machine tools. Int J Adv Manuf Technol 54(5–8):669–676

14. Jiang SY, Mao HB (2010) Investigation of variable optimum preload for a machine tool spindle. Int J Mach Tools Manuf 50(1):19–28

15. Chen DJ, Bonis M, Zhang FH, Shen D (2011) Thermal error of a hydrostatic spindle. Precis Eng 35(3):512–520

16. Wu JY, Li HL (2010) Method for improving FEA accuracy for CNC spindle system thermal characteristics. Tool Eng 44(3):30–33 (in Chinese)

17. Fan CL, Sun FR, Yang L (2008) A numerical method on inverse determination of heat transfer coefficient based on thermographic temperature measurement. Chin J Chem Eng 16(6):901–908

18. Rebay M, Arfaoui A, Mebarki G, Maad RB, Padet J (2010) Improvement of the pulsed photothermal technique for the measurement of the convective heat transfer coefficient. J Therm SCI 19(4):357–363

19. Xu M, Jiang SY, Cai Y (2007) An improved thermal model for machine tool bearings. Int J Mach Tools Manuf 47(1):53–62

20. Yu ZP, Lu Y (1995) Heat transfer theory. Higher Education Press, Beijing

21. Kitayama S, Kita K, Yamazaki K (2012) Optimization of variable blank holder force trajectory by sequential approximate optimization with RBF network. Int J Adv Manuf Technol 61(9–12):1067–1083

22. Chen T (2012) The FLR-PCFI-RBF approach for accurate and precise WIP level forecasting. Int J Adv Manuf Technol 63(9–12):1217–1226

23. Zhang PY, Lü TS, Song LB (2005) RBF networks-based inverse kinematics of 6R manipulator. Int J Adv Manuf Technol 26(1–2):144–147

24. Zhang HT, Yang JG, Zhang Y, Shen JH, Wang C (2011) Measurement and compensation for volumetric positioning errors of CNC machine tools considering thermal effect. Int J Adv Manuf Technol 55(1–4):275–283

25. Chen L (2008) Study on prediction of surface quality in machining process. J Mater Process Technol 205(1–3):439–450

26. Lu C, Ma N, Chen Z, Costes JP (2010) Pre-evaluation on surface profile in turning process based on cutting parameters. Int J Adv Manuf Technol 49(5–8):447–458